Available online at www.sciencedirect.com

Manufacturing Letters

Manufacturing Letters 00 (2023) 000–000

51st SME North American Manufacturing Research Conference (NAMRC 51, 2023)

A simulation-based analysis on the cooling effect and the tool temperature distribution in modulated turning (MT)

Mert Ozdemir[1], Burak Sencer[1]* and Yang Guo[2]

[1]*School of Mechanical, Industrial and Manufacturing Engineering, Oregon State University, Corvallis, OR, 97331, USA*
[2]*Department of Mechanical Engineering, Michigan State University, 428 S. Shaw Lane, East Lansing, MI 48824*

* Corresponding author. Tel.: +15417375919; *E-mail address:* Burak.Sencer@oregonstate.edu

---

Abstract

Modulation assistance is widely used for breaking chips of highly ductile materials in turning. This process is also known as the “modulated turning” (MT) or the “modulation assisted machining (MAM)”. The process transforms continuous single point turning into an intermittent cutting process where the tool tip briefly disengages from the workpiece generating discrete short chips. Resembling the milling process mechanics, periodic tool disengagements in modulated turning introduces cyclic cool-down periods and thus it can potentially attenuate tool-tip temperatures. It has been hypothesized that this effect can greatly lower maximum and the average tool-tip temperatures improving wear resistance of the process. This paper presents a thermal model to predict the tool-tip temperature distribution in modulated turning. A generalized chip formation formulation is first developed to predict the uncut chip thickness variation, cutting forces and the tool engagement/disengagement phase durations. Thermomechanical behavior of tool-chip contact is then modeled to predict the rake face temperature distribution. Simulation studies are presented to analyze the temperature distribution and understand peak temperature (hot) spots on the rake face. It has shown that the phase angle parameter – the frequency ratio between workpiece rotation and tool modulation– of MT plays a key role in controlling the hot spots on the rake and can be used as a tool to influence the wear regime.

Keywords: Modulated turning; cutting mechanics; temperature

---

1. Introduction

Modulated turning was initially proposed for robust chip breakage and chip evacuation in turning of ductile materials [1]. The first application of modulated turning dates back to 1998 when it was first applied in deep hole drilling by Sakurai et al.[2]. Mechanics of MT process has not changed much since then. In MT, the tool is modulated sinusoidally in feed direction. Depending on the modulation (vibration) frequency and the amplitude tool-tip disengages from the workpiece briefly transforming conventional continuous turning into intermittent turning process. As a result, discrete chip is generated, which solves the chip jam problem.

Typically, existing feed drives of the turning center is used to modulate the tool. Machine tool feed drives have limited bandwidth; and thus, modulated turning has been historically applied on the most power efficient operating condition where the modulation frequency is selected ½ of the spindle rotation frequency and the vibration (modulation) amplitude is set to 2x of the feed rate [3]. However, modern machine tool feed drives can provide much wider bandwidths allowing other modulation conditions, e.g., frequencies and amplitudes, to be applied in practice, which helps exploit other benefits of modulated turning as well [4].

For instance, low frequency tool modulations have potential to reduce average cutting temperature. Gao et al. [5] have measured the temperature distribution in the cutting zone and developed predictive models. They argued that average cutting temperature can be lowered in modulated turning. It should be emphasized that for shallow depth of cuts modulated turning can lower specific cutting energy improving machineability [6]. Yeung [7] was the first one to point that out. Later, Eren and Sencer [4] demonstrated such effect and explained the mechanism. At low depth of cuts, ploughing induced cutting becomes dominant in the shear mechanism and thus requires larger cutting energy. This is known as the well-known "size effect". However, when modulations are applied, maximum instantaneous uncut chip thickness becomes larger, i.e., in cases 2-4x greater than that of continuous cutting [8]. As a result, it overcomes the size effect and helps the process operate in more efficient shearing regime, which results in reducing overall cutting energy. Thus, although MT has potential to provide reduced cutting energy it does not necessarily has the ability to provide such advantage at all cutting conditions. Guo et al. have investigated tool-life in modulated machining of compact graphite iron (CGI) workpieces and reported that low frequency feed modulations can significantly improve the tool life [9,10] as compared to continuous cutting.

Dynamics of modulated turning process also differs greatly from the conventional continuous turning. Copenhaver et. al. [11] published the first report that MT has a stabilization effect and allows greater chatter stability margins. The main reason for attaining greater stability is assumed to be due to the tool disengagement from the workpiece. The "air-cutting phase" disturbs self-excited chatter vibrations and helps increase the chatter stability limits. Copenhaver and Schmitz [12] later utilized time-domain simulations to draw stability lobe diagrams (SLDs) of MT. Nam and Sencer, for the firs time, proposed a frequency domain-based approach to analytically predict the SLD of modulated turning [13]. More recently Eren and Sencer [8] have developed a semi-discrete time-domain model of the process to accurately predict the stability margins for any operating conditions. They demonstrated that MT can produce the highest stability not when the modulation frequency is selected ½ of the spindle rotation frequency, but actually when it is set much differently.

Based on these past works, it is understood that MT can provide great improvement on cutting mechanics and dynamics. To unlock some of these benefits, the operating parameters should be selected differently than the well-known typical (optimal) condition.

MT has the potential to improve thermal loads on the tool and yield lower tool tip temperature as well. But the effect of modulation parameters on the cutting temperature has never been thoroughly investigated. This paper, for the first time, provides a thermal model of the MT process and predicts cutting tool temperature for various modulation conditions. Through simulation studies, it generates new knowledge on how tool modulations affect overall temperature distribution on the tool and controls peak cutting temperature.

The paper is outlined as follows. First, a generalized model is presented to analytically predict the uncut chip thickness for any given modulation condition, which facilitates calculation of cutting forces and the energy. Next, a thermos dynamics model of the process is introduced, and an insightful simulation study is then presented.

2. Analysis of chip formation in MT

2.1. Kinematics of MT

Basic kinematics of the MT process has been already well presented in the past [14]. Here, it is briefly summarized for coherence, and the analytical chip thickness formation calculation is presented.

MT process applied in the face turning configuration is presented in Fig. 1. Tool is modulated in feed direction, and the tool tip trajectory is shown in Fig. 1b. Each modulation cycle of the tool is called as the "cutting cycle" in this work. $\rho_n(\theta)$ and $\rho_{n+1}(\theta)$ represent the tool-tip trajectory during the n^{th} and $(n+1)^{th}$ spindle revolutions, respectively. h_0 is the nominal (commanded) feedrate, whereas $h(\theta)$ becomes the time varying chip thickness, which is evaluated as follows.

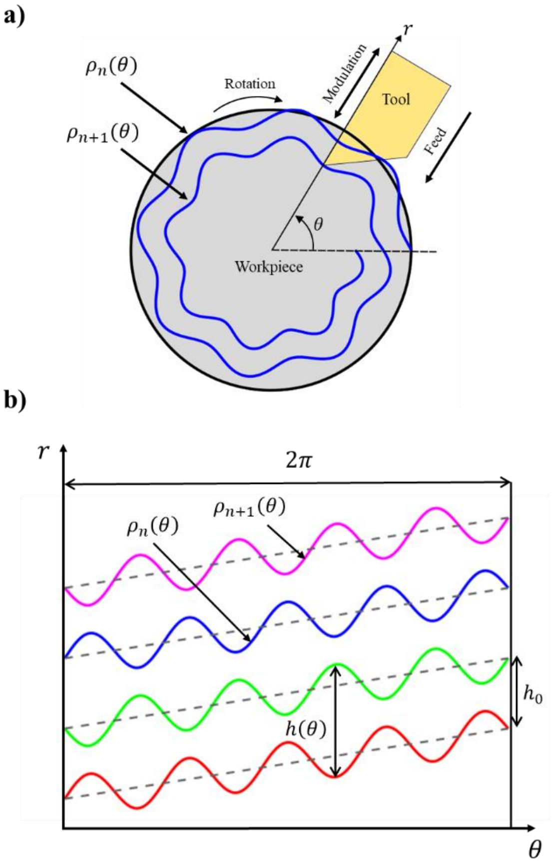

Fig. 1 (a) Schematic of turning process with tool modulations; (b) Projection of tool path into cylindrical coordinate system

Firstly, sinusoidal tool modulation is expressed as:

$$m(t) = A\sin\left(\frac{f_m}{f_w}\theta\right) \tag{1}$$

$$\theta = \theta(t) = 2\pi f_w t \tag{2}$$

where $\theta$is spindle rotation, A is modulation amplitude, f_m is the modulation frequency, and f_w is the spindle speed. Subtracting two consecutive tool trajectories yields $h(\theta)$ as:

$$\left.\begin{array}{c}\rho_{n+1} = nh_0 + \dfrac{h_0}{2\pi}\theta + A\sin\left(\dfrac{f_m}{f_w}\theta + n\phi\right)\\ \rho_n = (n-1)h_0 + \dfrac{h_0}{2\pi}\theta + A\sin\left(\dfrac{f_m}{f_w}\theta + (n-1)\phi\right)\\ h(\theta) = \rho_{n+1} - \rho_n\end{array}\right\} \quad (3)$$

Above, ϕ donates the "phase angle", which represents the shift in the tool trajectories in successive spindle revolutions and defined as [14]:

$$\phi = 2\pi\left(\frac{f_m}{f_w} - INT\left(\frac{f_m}{f_w}\right)\right), 0 \le \phi \le 2\pi \quad (4)$$

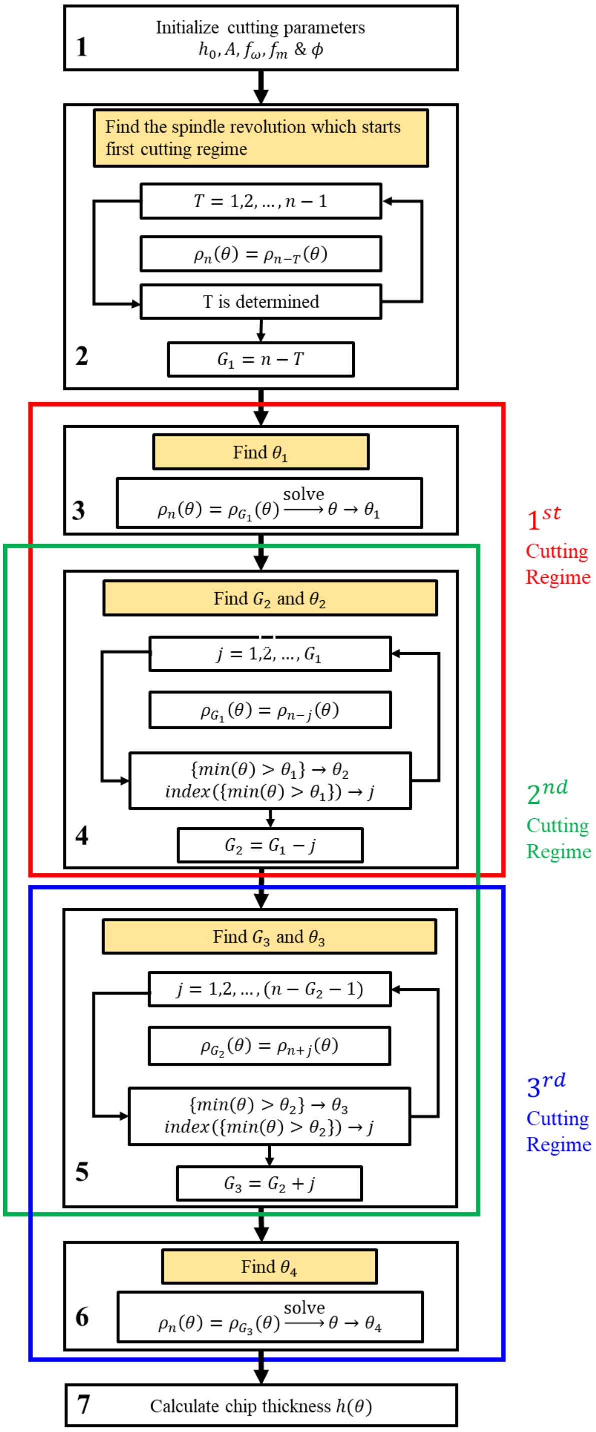

Fig. 2 Flow chart for analytical chip thickness calculation

where, $''INT[]''$ is the integer part of the ratio, and it indicates how many fully completed modulation waves are observed in one spindle revolution.

By setting $\phi \neq 0$ or 2π ensures that there exist an incomplete tool modulation wave within the spindle revolution, and thus tool trajectory continuously shifts ϕ over successive revolutions. The shift yields discrete chip formation, and for a given ϕ and A tool can leave the workpiece surface. The minimum condition to generate discrete chips, by ensuring that the n^{th} and $(n-1)^{th}$ spindle revolutions intersect, is found as [1]:

$$\rho_n(\theta) = \rho_{n-1}(\theta) \to A_{min} = \frac{h_0}{2sin\left(\frac{\phi}{2}\right)} \quad (5)$$

Notice that minimum modulation amplitude is achieved when the $\phi = \pi$. Modulation amplitude must be increased if larges phase angle is selected. In practice, phase angle can be set in the range of $\pi/2 < \phi < 3\pi/2$ to keep the modulation amplitude level low and thus the process can be applied in practice using conventional feed drives of machine tool [4].

3. Prediction of uncut chip thickness

Equation 5 presents the necessary condition to realize discrete chip generation. However, it does not present the maximum chip thickness (load). This section first provides a general formulation on how to analytically predict the chip thickness for any given A and ϕ, and the formulation is then validated for conditions when $\phi = \pi$,$2\pi/3$, and $\pi/2$.

3.1. Analytical prediction of uncut chip thickness

Tool trajectories that generate individual cutting regimes should be identified to accurately predict uncut chip thickness. Chip thickness is calculated by taking the difference of intersecting cutting cycles. It is known that [14]chip formation consists of 3 cutting regimes (sections) [14]. The idea is to determine which spindle revolutions form the chip thickness in those individual ship sections. presents the flow chart used to calculate chip thickness for any given phase angle and modulation amplitude.

The algorithm starts with inputting the cutting parameters as shown in Fig.2. Next, it is determined which past spindle revolutions initiate chip formation, i.e. intersect. Integer $T = 1,2,\dots,n-1$ is defined, and it is increased until

$$\rho_n(\theta) = \rho_{n-T}(\theta) \to \frac{T}{2\sin\left(\frac{T}{2}\phi\right)} \le \frac{A}{h_0} \quad (6)$$

is violated, which indicates that the cutting cycle in the (n^{th}) spindle revolution intersects with a cutting cycle within the one of the $(n-T)^{th}$ spindle revolution.

Past spindle revolutions that contribute to the first, second and third cutting regimes (chip formation portions) are denoted as G_1,G_2 and G_3 , respectively. As shown in Fig.2, once G_1 is determined (from Eq.6), starting point of the first cutting regime (chip section) θ_1 can be calculated from Eq.6 as well. Next, end point of this section of the chip, θ_2, can be found once the spindle revolutions that define the second portion of the chip is found. This is presented in the 4^{th} step of the flow chart. Intersection points of the G_1^{th} spindle revolution with past spindle revolutions are scanned. This is similar to the step

1 in the flow chart (See Fig.2). The smallest value of $\theta > \theta_1$ is assigned as the end point of first cutting regime and $\theta = \theta_2$ is set. The same procedure is applied to determine the spindle revolution that defines the 3rd cutting regime (G_3). Chip generation is periodic, and thus the starting point of off-cut region (θ_0) can be determined by subtracting the period of modulation $(1/f_m)$ from θ_4. The chip thickness function is then formulated as:

$$h(t) = \begin{Bmatrix} \rho_n(\theta) - \rho_{G_1}(\theta), \theta_1 \leq \theta < \theta_2 \\ \rho_n(\theta) - \rho_{G_2}(\theta), \theta_2 \leq \theta < \theta_3 \\ \rho_n(\theta) - \rho_{G_3}(\theta), \theta_3 \leq \theta \leq \theta_4 \end{Bmatrix} \tag{7}$$

An illustrative example is provided in Fig. 3. Modulation amplitude is set to $A = 2.25h_0$, and the phase angle is set to $\phi = 72$. As shown in Fig. 3, each chip (shaded area) consists of 3 portions. Note that *G₁* becomes *(n-3)th* spindle revolution, whereas *G₂* is *(n-2)th* revolution and *G₃* is *(n-1)th* revolution. The uncut chip thickness and air-cut & in-cut durations can be predicted for various phase angles and modulation amplitudes with the proposed method.

An important parameter is air-cutting ratio and defined as:

$$R_{OUT}\% = \frac{\theta_1 - \theta_0}{\theta_4 - \theta_0} \times 100 \tag{8}$$

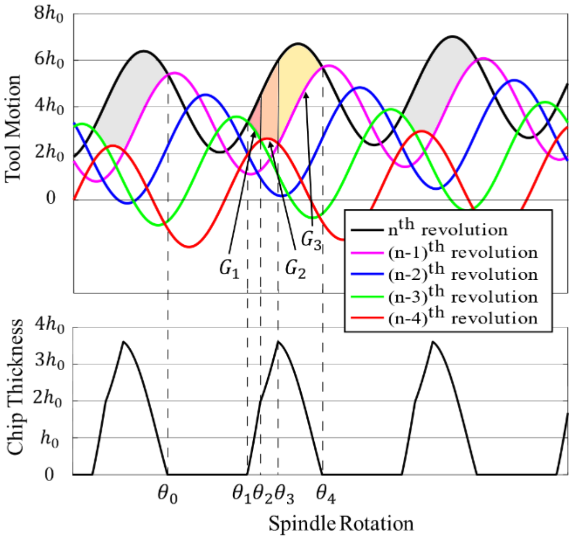

Fig. 3 Tool trajectories and chip formation for ϕ=72°

Fig. 4 presents the air-cutting ratio for all possible phase angles and modulation amplitudes. Air-cutting ratio controls the cooling effect in MT. The cutting parameters can be tuned accurately to achieve more robust chip generation and higher air cutting ratios by utilizing the proposed map.

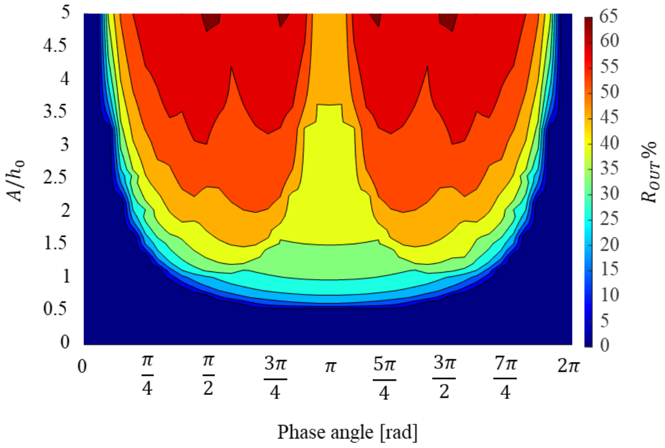

Fig. 4 Cutting duty cycle map

3.2. Chip thickness calculation for $\phi = \pi, 2\pi/3$ & $\pi/2$

Finally, proposed generalized uncut chip thickness prediction algorithm is demonstrated for cases when $\phi = \pi, 2\pi/3$ & $\pi/2$. Table 1 summarizes which spindle revolutions generate various sections of the chip. Fig. 5 illustrates examples of tool trajectories and corresponding chip generation for specified phase angles. For instance, when $\phi = \pi$, maximum chip thickness becomes, $\max h(\theta) = 2h_0$ and it is independent of the modulation amplitude since tool modulation from $(n-2)^{th}$ spindle revolution and the cutting cycle in the current spindle revolution are in phase. However, this condition is not valid for other cases. For instance, for $\phi = 2\pi/3$ if modulation amplitude is large enough, tool modulation from $(n-3)^{th}$ spindle revolution start to affects the uncut chip thickness and maximum chip thickness becomes 3x larger than the nominal feed rate. This is due to the fact that when one spindle revolution is completed, modulation cycle is one-third completed so that the cutting cycles in every three successive spindle revolutions become in phase. The same chip generation phenomenon is also observed when $\phi = \pi/2$. In this operating

Table 1 Chip formation regimes for various phase angles and modulation amplitudes

Chip formation for $\phi = \pi$				
Uncut Chip Thickness	$\theta \in [\theta_1, \theta_2)$	$\theta \in [\theta_2, \theta_3)$	$\theta \in [\theta_3, \theta_4)$	A/h_o Interval
$h(\theta) = \rho_n(\theta) - \rho_{n-j}(\theta), j = 1,2,1$	$\rho_n(\theta) \cap \rho_{n-1}(\theta)$	$\rho_n(\theta) \cap \rho_{n-2}(\theta)$	$\rho_n(\theta) \cap \rho_{n-1}(\theta)$	$\sigma_{crit} \leq A/h_0$
Chip formation for $\phi = 2\pi/3$				
Uncut Chip Thickness	$\theta \in [\theta_1, \theta_2)$	$\theta \in [\theta_2, \theta_3)$	$\theta \in [\theta_3, \theta_4)$	A/h_o Interval
$h(\theta) = \rho_n(\theta) - \rho_{n-j}(\theta), j = 1,2,1$	$\rho_n(\theta) \cap \rho_{n-1}(\theta)$	$\rho_n(\theta) \cap \rho_{n-2}(\theta)$	$\rho_n(\theta) \cap \rho_{n-1}(\theta)$	$0.577 \leq A/h_0 < 1.154$
$h(\theta) = \rho_n(\theta) - \rho_{n-j}(\theta), j = 2,3,1$	$\rho_n(\theta) \cap \rho_{n-2}(\theta)$	$\rho_n(\theta) \cap \rho_{n-3}(\theta)$	$\rho_n(\theta) \cap \rho_{n-1}(\theta)$	$1.154 \leq A/h_0$
Chip formation for $\phi = \pi/2$				
Uncut Chip Thickness	$\theta \in [\theta_1, \theta_2)$	$\theta \in [\theta_2, \theta_3)$	$\theta \in [\theta_3, \theta_4)$	A/h_o Interval
$h(\theta) = \rho_n(\theta) - \rho_{n-j}(\theta), j = 1,2,1$	$\rho_n(\theta) \cap \rho_{n-1}(\theta)$	$\rho_n(\theta) \cap \rho_{n-2}(\theta)$	$\rho_n(\theta) \cap \rho_{n-1}(\theta)$	$0.707 \leq A/h_0 < 1$
$h(\theta) = \rho_n(\theta) - \rho_{n-j}(\theta), j = 2,3,1$	$\rho_n(\theta) \cap \rho_{n-2}(\theta)$	$\rho_n(\theta) \cap \rho_{n-3}(\theta)$	$\rho_n(\theta) \cap \rho_{n-1}(\theta)$	$1 \leq A/h_0 < 2.236$
$h(\theta) = \rho_n(\theta) - \rho_{n-j}(\theta), j = 3,4,1$	$\rho_n(\theta) \cap \rho_{n-3}(\theta)$	$\rho_n(\theta) \cap \rho_{n-4}(\theta)$	$\rho_n(\theta) \cap \rho_{n-1}(\theta)$	$2.236 \leq A/h_0$

condition max $h(\theta) = 4h_0$ is observed since tool modulation from $(n-4)^{th}$ spindle revolution affects the current uncut chip thickness. As it can be seen from Table 1, any modulation amplitude which is greater than $A = 2.23h_0$ yields theoretical maximum chip thickness values for all cases.

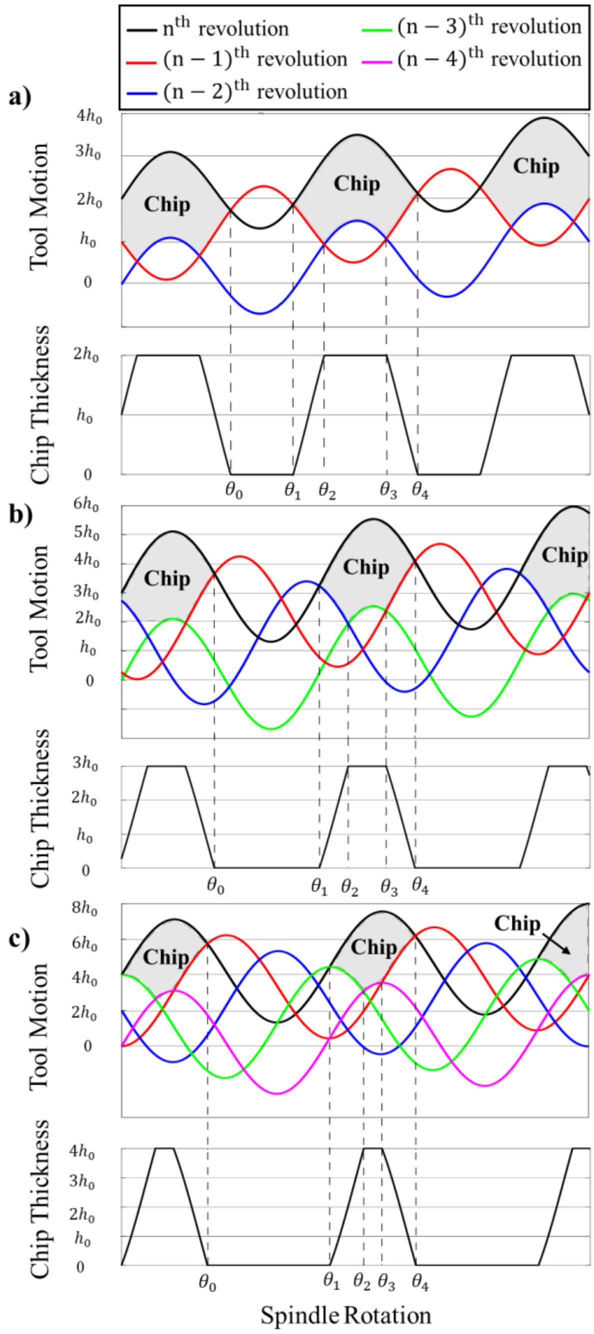

Fig. 5 Example of tool trajectories and chip formations for different phase angle values (a) ϕ=π; (b) ϕ=2π/3; (c) ϕ=π/2

4. Thermal model of MT

This section presents thermal model of MT process to predict the tool temperature. It is used to analyse and understand the cooling effect of MT process.

Firstly, the problem is simplified by modelling it based on fundamental orthogonal cutting kinematics. Note that such assumption is widely acceptable in face turning and plunge turning processes [15], which is the focus here. It is assumed that tool radius is close to zero and since tool flank does not touch workpiece, heat generation is not observed in the tertiary shear zone [16]. Heat transfer from chip to tool occurs only in rake face, which can be modelled via a dual-zone model [17].

4.1. Modeling of cutting force and power on the rake face

As material is deformed in primary shear zone, it exerts high normal pressure against the tool. This phenomenon yields sticking/sliding friction conditions at the regions on the tool tip, and shown in Fig.6. [17]Normal pressure decreases far away from tool tip and causes chip to slide over the tool with friction. Coulomb friction is assumed to be valid in order to model the shear stress in sliding region. Budak [18] argued that thermomechanical behaviour in sticking and sliding zones should be analysed separately.

Shear stress (τ) on the rake face is constant in the sticking region, and it is equal to the material shear stress [16]. In the sliding region, shear stress is proportional to the normal pressure, and sliding friction obeys coulomb friction law [19]. τ along the contact length is then defined as[17]:

$$\begin{aligned} \tau &= \tau_s &&, x < l_p \\ \tau &= \mu P(x) &&, l_p \le x \le l_c \end{aligned} \qquad (9)$$

where, l_p is the sticking length, l_c is the total contact length.

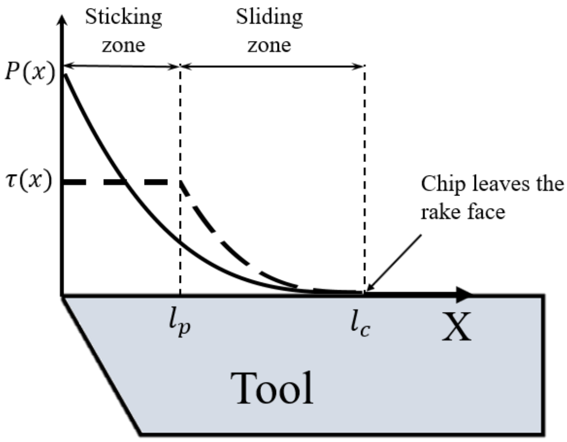

Fig. 6 Stress distributions on the rake face

Sticking and sliding lengths are influenced by the stress distributions; and they are first analysed as follows. Firstly, shear stress is a function of normal pressure and sliding friction coefficient in the sliding region. The normal pressure is modelled after [17]:

$$P(x) = P_0\left(1 - \frac{x}{l_c}\right)^{\zeta} \qquad (10)$$

where $\zeta = 3$ is set[20]. P_0 is the normal pressure at the tool tip. The normal force on the tool is calculated by integrating Eq.10:

$$F_v = \int_0^{l_c} P(x)dx = \int_0^{lc} P_0\left(1 - \frac{x}{l_c}\right)^{\zeta} bdx = P_0\frac{bl_c}{\zeta + 1} \qquad (11)$$

with b being is the width of cut. Note that normal force in orthogonal cutting can be simply calculated by using shear force acting on shear plane

$$F_v = F_s\frac{\cos(\lambda_a)}{\cos(\lambda_a - \alpha + \phi_c)} \qquad (12)$$

where, α is the rake angle, ϕ_c is the shear angle, and λ_a is the apparent friction angle, and shear force becomes

$$F_s = \tau_s \frac{bh}{\sin(\phi_c)} \tag{13}$$

assuming uniform stress distribution on shear plane. Combining Eqs. (10) – (13), P_0 is obtained as:

$$P_0 = \tau_s \frac{h(\zeta+1)}{l_c sin\phi_c} \frac{\cos(\lambda_a)}{\cos(\phi_c+\lambda_a-\alpha)} \tag{14}$$

Next, contact length is calculated considering the moment equilibrium at the tool tip. The moment created by normal force acting on shear plane (M_{NS}) at the tool tip must be equal to the moment created by the normal force acting on tool rake (M_{NT}):

$$M_{NS} = F_s \tan(\lambda_a - \alpha + \phi_c) \frac{h}{2\sin(\phi_c)} \tag{15}$$

$$M_{NT} = \int_0^{l_c} xP_0 \left(1-\frac{x}{l_c}\right)^{\zeta} bdx = F_s \frac{l_c}{\zeta+2} \frac{\cos(\lambda_a)}{\cos(\lambda_a-\alpha+\phi_c)} \tag{16}$$

Combining Eqs. (15)-(16), contact length is obtained as:

$$l_c = h\frac{\zeta+2}{2} \frac{\sin(\phi_c+\lambda_a-\alpha)}{\sin(\phi_c)\cos(\lambda_a)} \tag{17}$$

It is known that shear stress at the end of the sticking region equals to shear stress at the beginning of sliding region [17]. By using this compatibility, sticking length is derived as:

$$l_p = l_c \left[1-\left(\frac{\tau_s}{P_0\mu}\right)^{\frac{1}{\zeta}}\right] \tag{18}$$

where, F_u is the friction force acting on the tool, which can be derived as:

$$\left.\begin{aligned} F_u &= \int_0^{l_p} \tau_s bdx + \int_{l_p}^{l_c} \mu P_0 \left(1-\frac{x}{l_c}\right)^{\zeta} bdx \\ F_u &= \tau_s b\left(l_p + \frac{l_c}{\zeta+1}\right) \end{aligned}\right\} \tag{19}$$

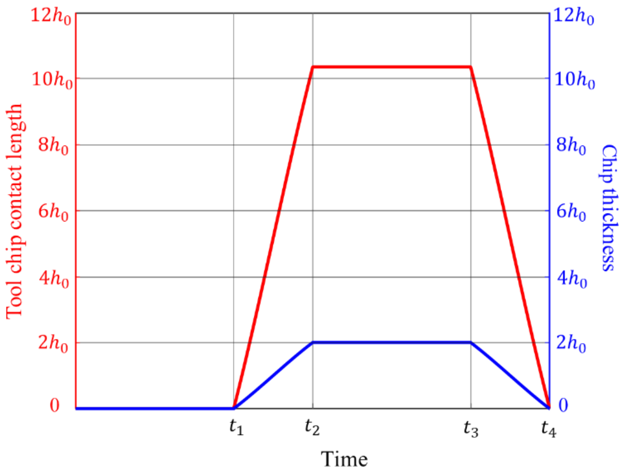

Fig. 7 Demonstration of variable chip thickness and contact length, the parameters used in the analysis; phase angle ϕ=π, A/h_0 =2, workpiece material Ti6Al4V, rake angle α=0°

Since Coulomb friction law is valid for orthogonal cutting, the apparent friction coefficient can be defined by utilizing Eqs. (11) and (19) as follows.

$$\mu_a = \tan(\lambda_a) = \frac{F_u}{F_v} = \frac{\tau_s}{P_0}\left[1+\zeta\left(1-\left(\frac{\tau_s}{P_0\mu}\right)^{\frac{1}{\zeta}}\right)\right] \tag{20}$$

where, μ is sliding friction coefficient. Ozel et al. [21] proposed that sliding friction can be taken as $\mu = 0.5$ for general turning processes and Eq.(20) can be solved iteratively. Thus, the τ_s/P_0 ratio can be obtained combining Eqs. (14) and (17) as:

$$\frac{\tau_s}{P_0} = \frac{\zeta+2}{4(\zeta+1)} \frac{\sin(2(\phi_c+\lambda_a-\alpha))}{(cos\lambda_a)^2} \tag{21}$$

As presented in the previous section, the uncut chip thickness is time varying in MT, i.e. $h = h(\theta) = h(t)$; and thus, contact length ($l_c(t)$) becomes time varying as well. Fig. 7 illustrates variation of contact length with respect to uncut chip thickness. Note that shear angle controls both the stress distribution and the contact lengths on the tip. Minimum energy principle proposed by Merchant [22] can be used to predict shear angle. Firstly, the apparent friction angle is computed for each shear angle value by Eq. (20). Tangential force and corresponding cutting power can then be calculated as

$$F_t = \tau_s \frac{bh}{\sin(\phi_c)} \frac{\cos(\lambda_a-\alpha)}{\cos(\phi_c+\lambda_a-\alpha)} \tag{22}$$

$$P_c = F_t V \tag{23}$$

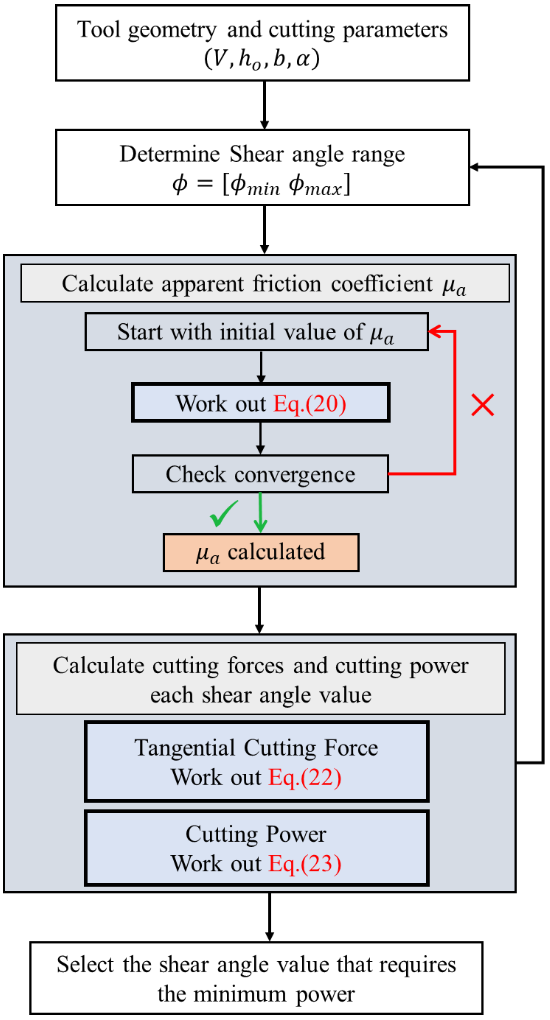

Fig. 8 Shear angle determination algorithm

Finally, the shear angle which results in minimum cutting power is predicted by Eq. (23) and the flow chart in Fig. 8 summarizes the shear angle prediction.

4.2. Modeling of heat flux

Once shear angle is calculated, stress distribution along the tool rake is found by using Eqs. (9) and (10). Chip velocity (V_c) controls the heat flux at the tool chip contact [19]Li et al. [23] proposed that chip velocity should be considered varying from tool tip to end of the sticking region. V_c is assumed as zero at the cutting edge. V_c at the end of sticking region and at the beginning of sliding region must be equal for continuity, and thus V_c is defined here as:

$$V_c(x) = \left\{ \begin{array}{ll} V\dfrac{sin\phi_c}{\cos(\phi_c-\alpha)}\left(\dfrac{x}{l_p}\right)^{\omega}, & 0 \le x < l_p \\ V\dfrac{sin\phi_c}{\cos(\phi_c-\alpha)}, & l_p \le x < l_c \\ 0, & x \ge l_c \end{array} \right\} \tag{24}$$

where the velocity distribution constant ω in the sticking region can be set to $\omega = 2$. Heat flux function along the contact length is expressed from Eq. 24 as:

$$q''(x) = \left\{ \begin{array}{ll} \tau_s V_c, & 0 \le x < l_p \\ \mu V_c P(x), & l_P \le x < l_c \\ 0, & x \ge l_c \end{array} \right\} \tag{25}$$

When the tool disengages from workpiece, heat generation stops. Unlike conventional turning [24], heat flux does not only vary spatially, but it also varies temporally as it becomes zero during the non-cutting periods. And thus, heat flux is defined as:

$$q''(x,t) = \left\{ \begin{array}{ll} 0, & t_0 \le t < t_1 \\ q''(x), & t_1 \le t < t_4 \end{array} \right\} \tag{26}$$

where t_0 is the starting point of non-cutting period, t_1 is the starting point of cutting period, and t_4 is the end point of cutting period. Fig. 9 presents variation of heat flux with respect to time and location on the tool tip (contact length).

4.3. Solution procedure

The cutting tool is exposed to time and space varying heat flux. If the thermal properties of the tool are independent of temperature, and the radiative heat transfer can be neglected, and the governing equation for heat transfer becomes [24]:

$$\frac{1}{\alpha_t}\frac{\partial T}{\partial t} - \nabla^2 T = S(x,y,t) \tag{27}$$

where, α_t is the thermal diffusivity of the cutting tool, ∇^2 denotes the second order partial derivative with respect to spatial coordinates. The right-hand side of Eq. 27, $S(x,y,t)$ term is called the source term. It presents effect of heat generation between the tool-chip contact and convective heat transfer.

Solution to Eq. 27 requires known initial and boundary conditions. Multi-variable heat flux function is one of the boundary conditions and varies with time and location. Since boundary conditions change with time, tool temperature modelling requires a transient solution. Here, MATLAB’s PDE Toolbox [25] is employed. The PDE Toolbox solves partial differential equations (PDEs) by using finite element analysis. The PDE Toolbox uses finite element method to discretize the problem domain into elements and solves the PDE by using iterative solution process [25].

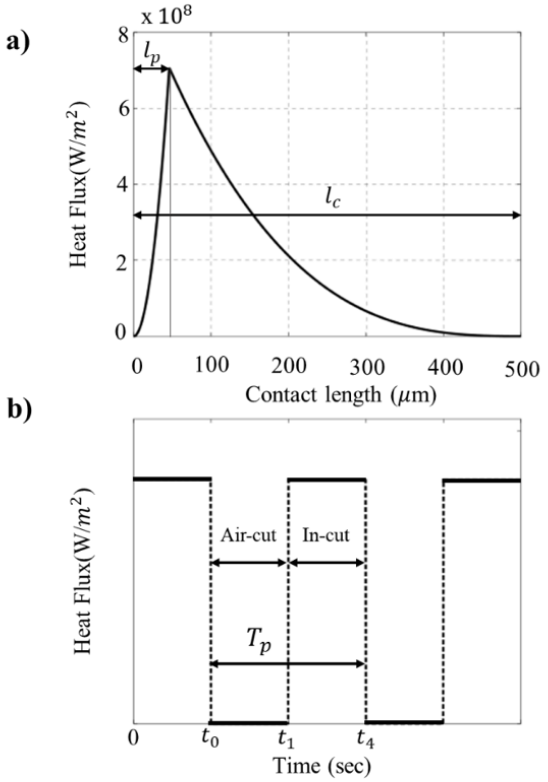

Fig. 9 (a) Variation of heat flux along the contact length; (b) Change of heat flux within the cutting and non-cutting periods

Heat generation between tool-chip is assumed to be uniform in the direction of the width of the cut. As a result, heat transfer problem becomes symmetric about a plane which is located at the midpoint of the width cut and parallel to side face of the tool. Tool tip can be modelled 2D by taking a cross section from plane of symmetry to decrease the computational cost, and Fig. 10 illustrates the model. Initial tool temperature is set to room temperature, and heat flux function $q''(x,t)$ is applied along the contact length as shown in Fig. 10. The heat flux can only flow into the tool along the contact length. Maximum contact length is calculated for each case. Then, the contact region is divided into several nodes to increase solution accuracy. The time varying contact length can be discretized into constant sections as shown in Fig. 11 and each section is considered.

Overall solution procedure is iterative and summarized in Fig. 12. First, nodes are assigned within contact length as convection boundary condition during air cutting. When tool engages the workpiece, heat flux is applied along the chip contact region depending on the contact length. For instance, when actual contact length becomes half of the maximum contact, half of the nodes in the contact region is exposed to heat flux, and the others are assigned as convection. When current chip thickness value achieves its maximum, contact length becomes maximum so that all the nodes in the contact region are exposed to heat flux. This procedure is applied during to all heating and cooling cycles.

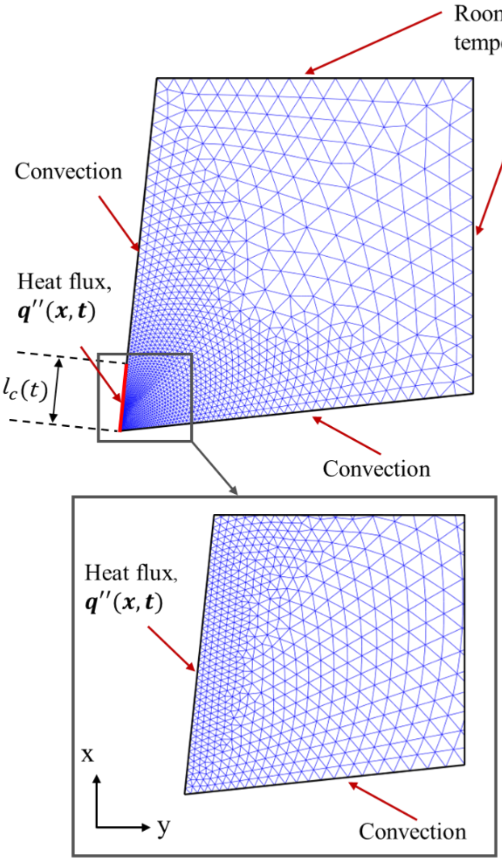

Fig. 10 Meshed tool geometry and applied boundary conditions

Table 2 Thermal properties of tool and workpiece materials

	Workpiece [26]	Tool[27]
Material	Ti6Al4V	TiN coated carbide tool
Density (kg/m^3)	4346	5420
Thermal conductivity (W/mK)	13.3	22
Specific heat capacity (J/kgK)	649	783.4

Table 3 Orthogonal cutting parameters

Rake angle (deg.)	12
Shear angle (deg.)	39
Apparent friction angle (deg.)	25
Sliding friction coefficient	0.5
Feedrate (mm/rev.)	0.1
Depth of cut (mm.)	1
Workpiece shear stress (MPa)	613
Cutting speed (m/min)	80
Percent time in-cut (%)	50

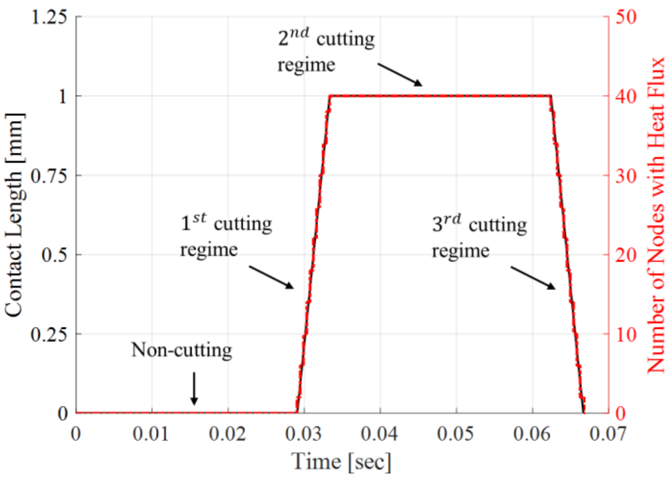

Fig. 11 Illustration of the discretization of contact length for MT for $\phi = \pi$, $A = 2.5h_0$ and $f_m = 3.5f_w$

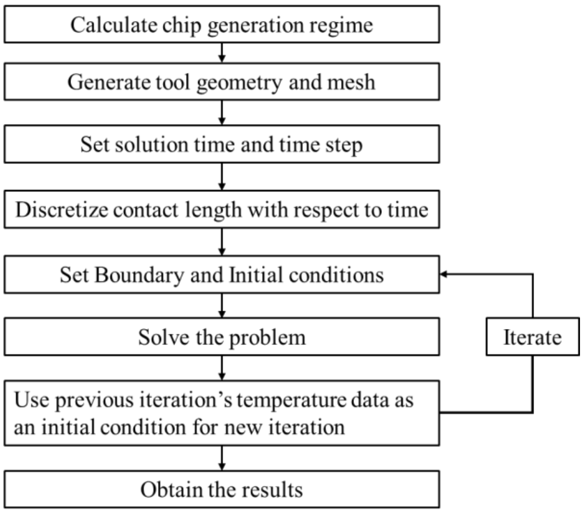

Fig. 12 Solution procedure for transient thermal problem

4.4. Validation of the proposed model

The developed model is validated against the experimental result provided by Armendia et al. [28] for an interrupted cutting process. Note that the process in [28] is not fully MT but very similar. The purpose is to ensure that the developed model can capture the thermal dynamics in interrupted cutting well. A series of experiments on Ti6Al4V alloy with coated carbide tool were carried out, and the transient cutting temperatures were measured by high bandwidth micro-thermal imaging system. Thermal properties of the tool and workpiece materials used in experiments are listed in Table 2. Table 3 shows the simulation input parameters to verify the proposed model, and Fig. 13 compares cutting temperatures.

It should be noted that a key aspect in accurately modeling tool temperature is determining suitable heat partition ratio (HPR) between the tool and chip for a process. HPR depends on the contact conditions, cutting speed, feed, surface roughness, temperature and time-dependent thermal properties of the tool and workpiece materials. An average HPR to cutting tool is determined through use of an inverse iterative method in this study [29]. This method involves comparing the maximum temperature values obtained from the experimental and simulated results. In this work, the heat partition ratio is set to 5.3%.

Temperature comparison presented in Fig. 13 presents accuracy of the developed model. The tool is heated up to 400 ℃ in 58.8 ms during the cutting period, and it cools down to 150 ℃ at the same duration in the air cutting period. Proposed model captures it accurately.

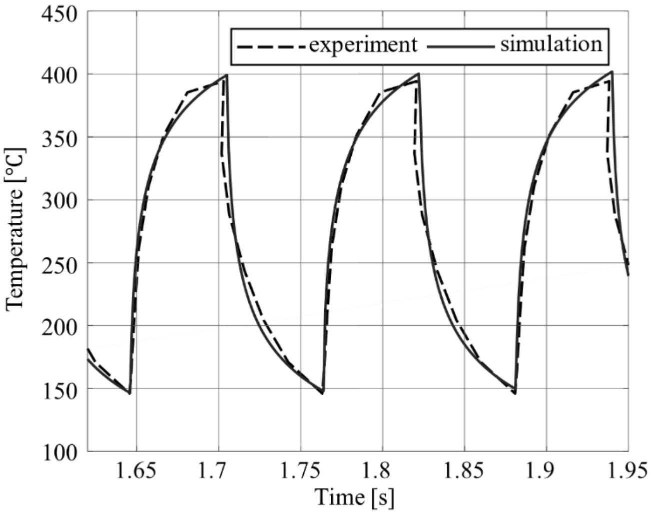

Fig. 13 Comparison of the simulation results and experimental measurements for TiN-coated carbide tool and Ti6Al4V workpiece. Cutting conditions: rake angle=12°, cutting speed V=80 m/min, feedrate f = 0.1 mm/rev

5. Tool tip temperature analysis

Accuracy of the model is validated in the previous section. Next, tool-tip temperatures and the cooling effect of MT are then analysed for $\phi = 180°, 120°, 90°$ in simulations using the proposed model. Tool and workpiece materials were selected identical to those used in experiments [28], and thermal properties of them shown in Table 2. Table 4 details the cutting conditions. The cutting parameters (spindle speed, modulation frequency and modulation amplitude) change the chip formation, which in turn changes the cutting forces and tool temperature due to the nature of the MT. While the phase difference is the function of spindle speed and modulation frequency, the maximum chip thickness value depends on the phase difference and modulation amplitudes. Gao et. al. [5] states that $\phi = 180°$ is the optimal modulation condition. Nevertheless, Eren et.al [8] showed that $\phi = 90°$ case requires the minimum specific cutting energy. The effect of setting phase difference as $\phi = 120°$ has never been studied for MT in the past. It should be noted that phase difference does not change the material removal rate, it affects air cutting ratio. In other words, tool-workpiece disengagement duration which has a great effect on tool cooldown can be changed by only changing modulation frequency. As it is explained in the Section 3, selecting phase difference values that is 1/2, 1/3 and 1/4 of 360° causes maximum chip thickness 2,3 and 4 times of nominal feedrate if a specific value of A/h_0 ratio is set. Table 1 summarizes the chip formation regimes for $\phi = 180°, 120°, 90°$ and different A/h_0. Therefore, modulation amplitude is set to $2.5h_0$. The material removal rates and cutting speeds are kept identical for all the conditions including the ordinary (continuous) turning. The transient heat transfer problem is solved for all cases to predict the tool tip temperature variation and its extremum. Since the process is transient for MT, temperature distribution along the rake face changes with respect to time. The temperature distribution along the rake face for $\phi = \pi$ is presented in Fig. 14.

Table 4 Cutting Parameters for each case

Parameters	Continuous turning	MT-Case 1	MT-Case 2	MT-Case 3
Phase difference (°)	0	180	120	90
Spindle speed (Hz)	40	40	40	40
Modulation frequency (Hz)	-	140	$133.\overline{3}$	130
Nominal feedrate (mm/rev)	0.1	0.1	0.1	0.1
Modulation amplitude (mm)	-	0.25	0.25	0.25
Cutting speed (m/min)	300	300	300	300
Maximum chip thickness (mm)	0.1	0.2	0.3	0.4

As show in Fig. 14, maximum temperature is observed after the second cutting regime, because at this instant the largest contact length is observed that yields maximum energy input. Temperature distributions along the contact length at these instants are plotted in Fig. 15 to determine the peak temperature points on the tool for each case.

As shown in Fig. 15, peak tool tip temperature location varies based on the cutting conditions in MT. Firstly, peak temperature is observed at 0.09 [mm] from the cutting edge for conventional continuous (ordinary) turning. For MT, peak temperature location is predicted at 0.18[mm], 0.27[mm] and 0.33 [mm] from the tool's cutting edge when $\phi = 180°, 120°, 90°$, respectively.

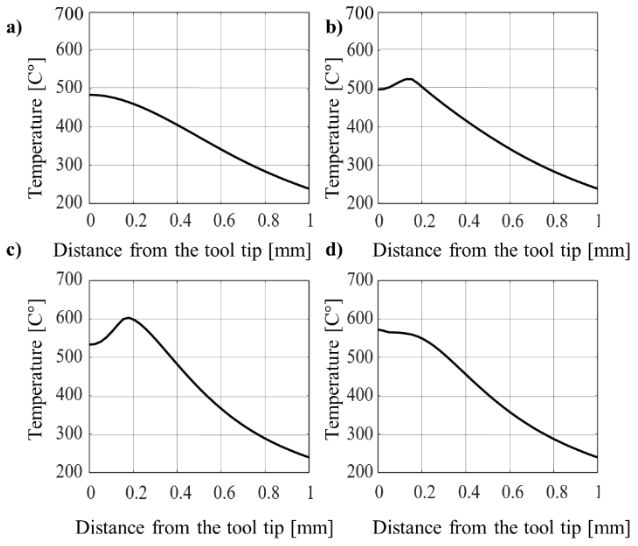

Fig. 14 Variation of temperature distribution along the rake face in one modulation; a) After non-cutting period; b) After first cutting regime; c) After second cutting regime; d) After third cutting regime

The reason for this difference can be explained by varying heat flux along the contact length. As shown in Fig. 9, maximum value of heat flux is predicted at the end of sticking region. As can be seen in Eq. 17 and 18, the contact length changes based on instantaneous chip thickness, and the length of the sticking region changes accordingly as well. Since the maximum chip thickness is 2, 3, and 4x of the nominal feedrate for $\phi = 180°, 120°, 90°$, the length of sticking region becomes approximately 2, 3, and 4 times greater than continuous turning. This relationship is key in controlling the maximum temperature locations on the tool tip. Temperature and time history for those locations are given in Fig. 16-18.

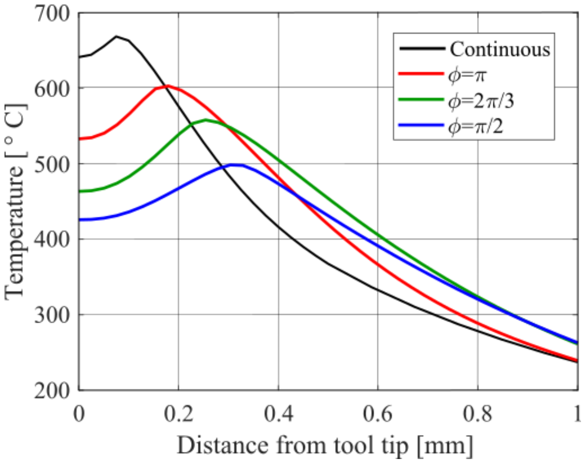

Fig. 15 Distribution of temperature along the rake face for different cases

Periodically heating cooling cycles occur when interrupted cutting is realized with MT. Although the heat flux remains constant, the amount of heat input increases during the heating period in comparison to continuous cutting while the same amount of material is removed. This caused by the enlarged contact surface of tool and workpiece as shown in Fig. 5. When the cutting tool lost its contact with the workpiece (cooling period), tool temperature decreases because heat generation does not occur. The effect of interrupted cutting on tool temperature for different locations is shown in Fig. 16-18. The duration of the heating and cooling periods depends on the modulation parameters. For a phase difference resulting in a high air cutting ratio, the cooling time increases. In this way, a decrease in tool temperatures is observed.

As shown in Fig. 16-18 temperatures observed in MT exceed conventional turning further away from the tool tip. This is expected since tool temperature decreases in conventional turning due to low heat flux away from tool tip and the effect of convection. In addition, maximum contact length in MT is greater than maximum contact length in conventional turning. Hence, the maximum value of heat flux in MT is observed further away from tool tip as compared to conventional turning. Investigating the maximum temperatures for all cases is a good way to understand the effect of cooling in MT. Table 5 shows maximum temperatures on the tool rake face for all the cases.

Table 5 Maximum tool temperatures for each case

	Temperature (℃)
Continuous turning	711.96
MT - Case 1 ($\phi = 180°$)	711.30
MT - Case 2 ($\phi = 120°$)	662.22
MT - Case 3 ($\phi = 90°$)	622.64

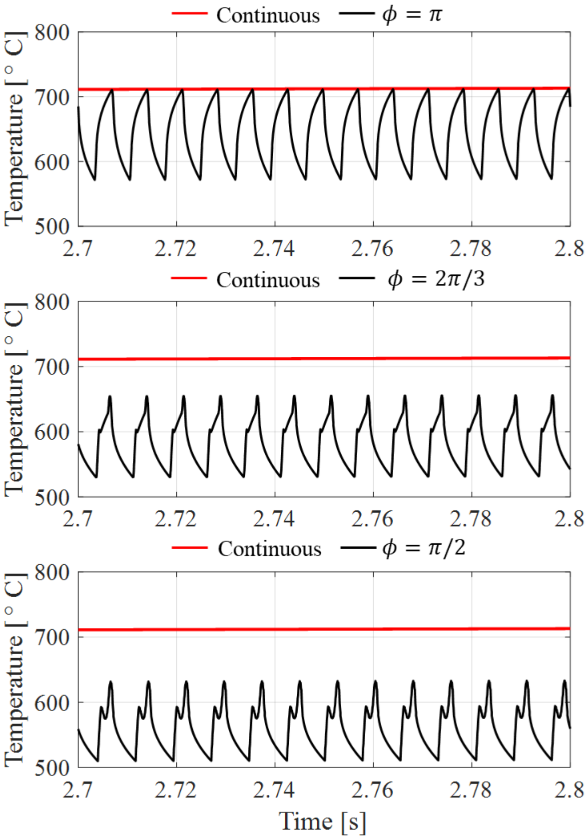

Fig. 16 Simulated rake face temperature simulated at x=0.18 [mm] from the tool tip.

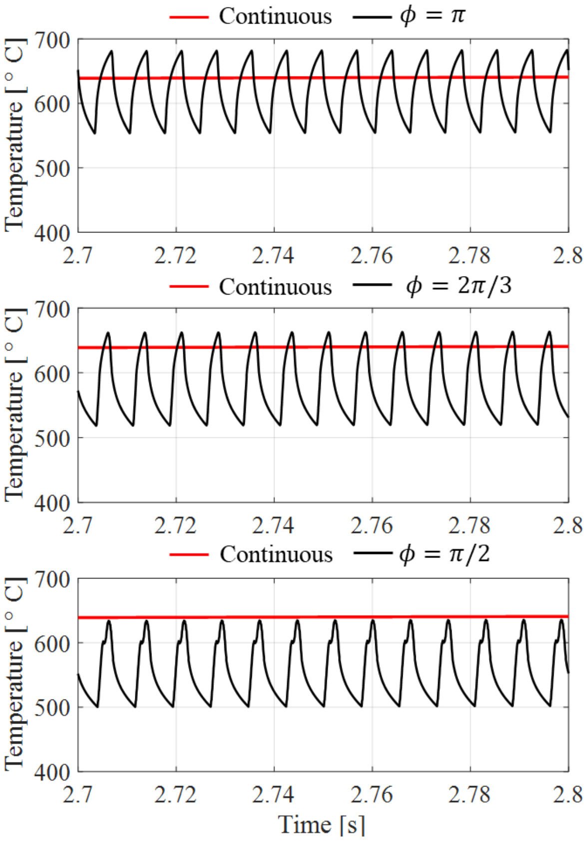

Fig. 17 Simulated rake face temperature at x=0.27 [mm] from the tip.

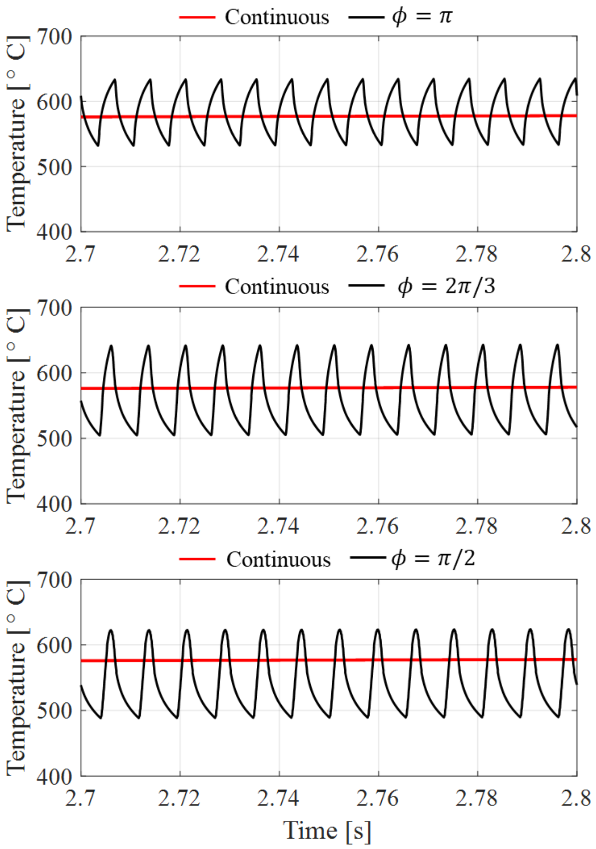

Fig. 18 Simulated rake face temperature at x=0.33 [mm] from tool tip

As shown in Table 5, the maximum temperature on tool rake face in conventional (continuous) turning is greater than all other cases. When MT is applied, interrupted cutting is realized, and maximum temperature on tool rake face decreases. It should be noted that phase angle has a significant effect on maximum tool temperature. As phase angle changes from $\phi = 180°$ to $\phi = 90°$, the maximum temperature decreases around 90℃ for cutting parameters specified above. This situation is caused by effect of air-cutting ratio. Although maximum chip thickness occurs in $\phi = 90°$, minimum value of maximum temperatures is observed at this phase angle since air-cut duration is maximum.

6. Conclusions & Future Work

This paper presented a transient tool temperature prediction for the MT process. The proposed method takes into effect of variable uncut chip thickness for different phase angles. Heat flux was calculated analytically by using dual zone model. A numerical approach was used to solve the transient heat transfer problem, namely finite element method. Tool temperature is higher at close the tool-tip during continuous turning. MT provides larger temperature further away from the tool tip. It can be understood that MT distributes cutting energy along the rake face, and thus it prevents accumulation of energy in a specific location such as at the tool-tip. The tool temperatures experience fluctuating trend in MT because of its discrete cutting kinematics. The effects of modulation parameters on temperature are investigated. The lowest maximum temperature is observed when phase angle is $\phi = 90^0$.

The proposed method in this work has some limitations. Firstly, the simulations have been run for 2D orthogonal cutting model. Secondly, heat partition ratio between tool and chip interface assumed as 5.3%. This assumption should be validated with experiments. Finally, effect of tertiary deformation zone will be considered as future work.

Acknowledgements

This research is supported by US's National Science Foundation (NSF Award no: 2019370).

Nomenclature

A	Modulation amplitude (m)
b	Width of cut (m)
F_s	Shear force (N)
F_t	Tangential force (N)
F_u	Friction force (N)
F_v	Normal force (N)
f_m	Modulation frequency (Hz)
f_w	Spindle speed (Hz)
h_o	Nominal feedrate (m/rev)
h	Instantaneous uncut chip thickness (m)
l_c	Tool-chip contact length (m)
l_p	Length of sticking region (m)
P_c	Cutting power (W)
P_0	Pressure at tool tip (Pa)
P(x)	Pressure distribution of rake face (Pa)
q''	Heat flux (W/m^2)
S	Source term in heat balance equation
t	Time (s)
V_c	Chip velocity (m/s)
V	Cutting velocity (m/s)
α_t	Thermal diffusivity (m^2/s)
α	Rake angle (rad)
ζ	Pressure distribution exponent
θ	Spindle rotation angle (rad)
λ_a	Apparent friction angle (rad)
μ_a	Apparent friction coefficient
μ	Sliding friction coefficient
ρ_n	Tool position in nth spindle revolution (m)
τ_s	Material shear stress (Pa)
τ	Shear stress on tool rake face (Pa)
ϕ_c	Shear angle (rad)
ϕ	Phase difference (rad)
ω	Velocity distribution constant

References

[1] Mann, J. B., Guo, Y., Saldana, C., Compton, W. D., and Chandrasekar, S., 2011, "Enhancing Material Removal Processes Using Modulation-Assisted Machining," Tribol Int, **44**(10), pp. 1225–1235.

[2] Sakurai,Keizo: Adachi, Katsushige: Hanasaki, S., 1998, "Breaking Mechanism of Chips in Intermittently Decelerated Feed Drilling of Aluminum Alloys," Journal of Japan Institute of Light Metals, **48**(4), pp. 195–198.

[3] Mann, J. B., Saldana, C., Chandrasekar, S., Compton, W. D., and Trumble, K. P., 2007, "Metal Particulate

Production by Modulation-Assisted Machining," Scr Mater, **57**(10), pp. 909–912.

[4] Eren, B., and Sencer, B., 2020, "Mechanistic Cutting Force Model and Specific Cutting Energy Prediction for Modulation Assisted Machining," Procedia Manuf, **48**, pp. 474–484.

[5] Gao, Y., Mann, J. B., Chandrasekar, S., Sun, R., and Leopold, J., 2017, "Modelling of Tool Temperature in Modulation-Assisted Machining," Procedia CIRP, **58**(December), pp. 204–209.

[6] Yeung, H., Guo, Y., Mann, J. B., Compton, W. D., and Chandrasekar, S., 2016, "Effect of Low-Frequency Modulation on Deformation and Material Flow in Cutting of Metals," J Tribol, **138**(1), pp. 1–9.

[7] Mann, J. B., Guo, Y., Saldana, C., Yeung, H., Compton, W. D., and Chandrasekar, S., 2011, "Modulation-Assisted Machining: A New Paradigm in Material Removal Processes," Adv Mat Res, **223**, pp. 514–522.

[8] Eren, B., Nam, S., and Sencer, B., 2022, "Generalized Mechanics and Dynamics of Modulated Turning," J Mater Process Technol, **308**(July), p. 117708.

[9] Guo, Y., Stalbaum, T., Mann, J., Yeung, H., and Chandrasekar, S., 2013, "Modulation-Assisted High Speed Machining of Compacted Graphite Iron (CGI)," J Manuf Process, **15**(4), pp. 426–431.

[10] Sandoval, J., Ali, A., Kwon, P., Stephenson, D., and Guo, Y., 2023, "Wear Reduction Mechanisms in Modulated Turning of Compacted Graphite Iron with Coated Carbide Tool," Tribol Int, **178**, p. 108062.

[11] Copenhaver, R., Schmitz, T., and Smith, S., 2018, "Stability Analysis of Modulated Tool Path Turning," CIRP Annals, **67**(1), pp. 49–52.

[12] Copenhaver, R., and Schmitz, T., 2020, "Modeling and Simulation of Modulated Tool Path (MTP) Turning Stability," Manuf Lett, **24**, pp. 67–71.

[13] Nam, S., Eren, B., Hayasaka, T., Sencer, B., and Shamoto, E., 2021, "Analytical Prediction of Chatter Stability for Modulated Turning," Int J Mach Tools Manuf, **165**(November 2020), p. 103739.

[14] Gao, Y., Sun, R. L., Chen, Y. N., and Leopold, J., 2016, "Mechanical and Thermal Modeling of Modulation-Assisted Machining," International Journal of Advanced Manufacturing Technology, **86**(9–12), pp. 2945–2959.

[15] Putz, M., Oppermann, C., Bräunig, M., and Karagüzel, U., 2017, "Heat Sources and Fluxes in Milling: Comparison of Numerical, Analytical and Experimental Results," Procedia CIRP, **58**, pp. 97–103.

[16] Altintas, Y., 2012, *Manufacturing Automation: Metal Cutting Mechanics, Machine Tool Vibrations, and CNC Design*, Cambridge University Press.

[17] Ozlu, E., Molinari, A., and Budak, E., 2010, "Two-Zone Analytical Contact Model Applied to Orthogonal Cutting," Machining Science and Technology, **14**(3), pp. 323–343.

[18] Budak, E., and Ozlu, E., 2008, "Development of a Thermomechanical Cutting Process Model for Machining Process Simulations," CIRP Ann Manuf Technol, **57**(1), pp. 97–100.

[19] Karaguzel, U., 2021, "Transient Multi-Domain Thermal Modeling of Interrupted Cutting with Coated Tools," International Journal of Advanced Manufacturing Technology, **116**(1–2), pp. 345–361.

[20] Karaguzel, U., and Budak, E., 2018, "Investigating Effects of Milling Conditions on Cutting Temperatures through Analytical and Experimental Methods," J Mater Process Technol, **262**(November 2017), pp. 532–540.

[21] Özel, T., Sima, M., Srivastava, A. K., and Kaftanoglu, B., 2010, "Investigations on the Effects of Multi-Layered Coated Inserts in Machining Ti-6Al-4V Alloy with Experiments and Finite Element Simulations," CIRP Ann Manuf Technol, **59**(1), pp. 77–82.

[22] Merchant, M. E., 1945, "Mechanics of the Metal Cutting Process. II. Plasticity Conditions in Orthogonal Cutting," J Appl Phys, **16**(6), pp. 318–324.

[23] Li, L., Li, B., Ehmann, K. F., and Li, X., 2013, "A Thermo-Mechanical Model of Dry Orthogonal Cutting and Its Experimental Validation through Embedded Micro-Scale Thin Film Thermocouple Arrays in PCBN Tooling," Int J Mach Tools Manuf, **70**, pp. 70–87.

[24] Stephenson, D. A., and Ali, A., 1992, "Tool Temperatures in Interrupted Metal Cutting," Journal of Manufacturing Science and Engineering, Transactions of the ASME, **114**(2), pp. 127–136.

[25] Mathworks, C., 2014, "Partial Differential Equation Toolbox TM User ' s Guide R 2014 b."

[26] Mills, K. C., 2002, "Ti: Ti-6 Al-4 V (IMI 318)," *Recommended Values of Thermophysical Properties for Selected Commercial Alloys*, K.C. Mills, ed., Woodhead Publishing, pp. 211–217.

[27] Abukhshim, N. A., Mativenga, P. T., and Sheikh, M. A., 2005, "Investigation of Heat Partition in High Speed Turning of High Strength Alloy Steel," Int J Mach Tools Manuf, **45**(15), pp. 1687–1695.

[28] Armendia, M., Garay, A., Villar, A., Davies, M. A., and Arrazola, P. J., 2010, "High Bandwidth Temperature Measurement in Interrupted Cutting of Difficult to Machine Materials," CIRP Ann Manuf Technol, **59**(1), pp. 97–100.

[29] Chen, W.-C., Tsao, C.-C., and Liang, P.-W., 1997, "Determination of Temperature Distributions on the Rake Face of Cutting Tools Using a Remote Method," International Communications in Heat and Mass Transfer, **24**(2), pp. 161–170.